

Spin crossover in FeO under shock compression

Lélia Libon^{1,2*}, Alessandra Ravasio^{3*}, Silvia Pandolfi¹,
Yanyao Zhang⁴, Xuehui Wei⁵, Jean-Alexis Hernandez⁶,
Hong Yang^{4,5}, Amanda J. Chen⁴, Tommaso Vinci³,
Alessandra Benuzzi-Mounaix³, Clemens Prescher⁷,
François Soubiran⁸, Hae Ja Lee⁹, Eric Galtier⁹, Nick Czapla⁹,
Wendy L. Mao^{4,9}, Arianna E. Gleason^{4,9}, Sang Heon Shim⁵,
Roberto Alonso-Mori⁹, Guillaume Morard^{1,2*}

^{1*}Institut de Minéralogie, de Physique des Matériaux et de
Cosmochimie, Sorbonne Université, Muséum National d'Histoire
Naturelle, UMR CNRS 7590, 4 Place Jussieu, Paris, 75005, France.

²ISTerre, Université Grenoble Alpes, CNRS, Grenoble, 38000, France.

³Laboratoire pour l'Utilisation des Lasers Intenses (LULI), Ecole
Polytechnique, CNRS, CEA, Sorbonne Université, Palaiseau, 91128,
France.

⁴Earth and Planetary Sciences, Stanford University, Stanford, 94305,
CA, USA.

⁵School of Earth and Space Exploration, Arizona State University,
Tempe, 85287, AZ, USA.

⁶European Synchrotron Radiation Facility, Grenoble, France.

⁷Institut für Geo- und Umweltwissenschaften,
Albert-Ludwigs-Universität Freiburg, Freiburg, 79104, Germany.

⁸CEA/DAM Ile-de-France, ArpaJon, 91297, France.

⁹SLAC National Accelerator Laboratory 2575 Sand Hill Rd., Menlo
Park, 94025,, CA, USA.

*Corresponding author(s). E-mail(s): llibon@carnegiescience.edu;
alessandra.ravasio@polytechnique.edu; guillaume.morard@cnrs.fr;

Contributing authors: robertoa@slac.stanford.edu;

Abstract

FeO (wüstite), which exhibits complex electronic and structural properties with increasing pressure and temperature, is a key mineralogical phase for understanding deep planetary interiors. However, direct measurements of its spin state at high-pressure and temperature remain challenging in static compression experiments. Here, we employ laser-driven shock compression to extend the FeO principal Hugoniot up to ~ 900 GPa and perform in situ X-ray diffraction and X-ray emission spectroscopy up to 250 GPa, probing FeO's crystal structure and spin state. We demonstrate a continuous spin crossover of iron in FeO over a broad pressure range, with the high-spin state persisting beyond Earth's core-mantle boundary (CMB) conditions. These observations provide new experimental constraints on iron spin state at extreme conditions essential for geophysical models of (exo)planetary interiors.

Keywords: FeO, Wüstite, Spin transition, Laser-driven shock compression

FeO (Fe_xO , $0.9 < x < 0.98$), also known as wüstite, is a key phase in the Earth's mantle and core. Its physical and chemical behavior under extreme pressure-temperature conditions has been the subject of extensive research due to its significant implications for understanding the structure and evolution of the Earth and for Earth-like planets (Coppari et al, 2021; Mao et al, 1996; Hazen and Jeanloz, 1984). It represents the iron-rich end-member of ferropericlae (Mg, Fe)O, the second most abundant mineral in the lower mantle (Morard et al, 2017; McCammon et al, 1983), and is believed to occur in iron-enriched layers near the core-mantle boundary (CMB) due to partial melting or chemical segregation. Experimental and theoretical studies further suggest that an FeO-rich layer may also have formed through the fractional crystallization of a primordial basal magma ocean (Boukaré et al, 2025, 2015) or through core-mantle chemical interactions (Hirose et al, 2017; Manga and Jeanloz, 1996; Knittle and Jeanloz, 1991). Additionally, seismic observations, combined with experimental constraints, suggest that ultra-low velocity zones (ULVZs) can be explained by highly FeO-rich solid materials (Jackson and Thomas, 2021; Dobrosavljevic et al, 2019; Wicks et al, 2017, 2010; Ohta et al, 2014; Nomura et al, 2011; Labrosse et al, 2007). FeO is also central to understand the core composition, as oxygen is one of the main light elements in the

core (Komabayashi, 2014; Badro et al, 2007; Alfè et al, 2002, 1999; Ringwood, 1977). Thus, its physical properties at extreme conditions have significant implications for the structure, dynamics, and long-term evolution of planetary interiors.

Despite being a simple binary oxide, FeO exhibits a complex phase diagram, undergoing multiple pressure-induced structural transitions from NaCl-type B1 structure ($Fm\bar{3}m$) to rhombohedral rB1 phase ($R\bar{3}m$) at 16-27 GPa at ambient temperature (Jacobsen et al, 2005; Yagi et al, 1985), to the NiAs-type B8 phase ($P6_3/mmc$) >70 GPa (Murakami et al, 2004; Mao et al, 1996; Ozawa et al, 2010; Fischer et al, 2011b). At >250 GPa and >2000 K, FeO adopts the CsCl-type cubic B2 structure (Coppari et al, 2021; Ozawa et al, 2011b). More recently, Li et al (2024) reported a monoclinic mP4 phase ($P2_1/m$ space group) at around \sim 80 GPa on quenched sample after heating, revealing further complexity to the high-pressure diagram of FeO.

FeO also exhibits pressure-induced electronic transitions. First, an insulator-to-metal transition (IMT) in the B1 phase has been experimentally investigated at \sim 30-90 GPa and \sim 2600-1400 K (Fischer et al, 2011a; Ohta et al, 2012). Recently, however, it has been argued that instead of a sharp transition, FeO-B1 enters a broad quantum critical state between its insulating and metallic states (Ho et al, 2024), which could account for the electrical conductivity changes observed experimentally (Ohta et al, 2012). Second, FeO undergoes a spin transition from high-spin (HS) to low-spin (LS) iron (Hamada et al, 2016; Ozawa et al, 2011b,a; Badro et al, 1999; Pasternak et al, 1997). In the solid state, this transition can lead to a 20 to 40 % reduction in the ionic volume of iron and affect FeO's compressibility, density, and bulk modulus (Greenberg et al, 2023; Pasternak et al, 1997). In the liquid state, LS Fe-O bonds are shorter than in the HS state, resulting in a denser liquid relative to its HS equivalent (Morard et al, 2022; Hamada et al, 2016).

Additionally, LS iron appears to preferentially partition into the liquid phase, enhancing iron diffusion, particularly within ULVZs (Lin et al, 2013; Manga and Jeanloz, 1996), which may contribute to the stabilization of a dense, Fe-rich liquid layer at the core–mantle boundary (CMB) within a basal magma ocean (Labrosse et al, 2007). These processes have major implications for the long-term evolution of Earth’s deep interior, influencing mantle convection, core dynamics, and chemical exchange across the CMB. Thus, constraining the spin state of iron and its depth-dependent evolution is essential for developing accurate models of Earth’s inner structure and evolution.

Previous studies have suggested that the iron spin transition is directly coupled to the IMT transition (Leonov, 2015; Ohta et al, 2012; Cohen et al, 1997). Following the recent work of Ho et al (2024), the relationship between these two transitions depends on temperature: at lower temperatures, the IMT can proceed via closure of the t_{2g} gap prior to spin crossover, whereas at higher temperatures, the metallization occurs through the closure of the e_g gap, which simultaneously triggers the spin crossover, implying that spin and electronic transitions may become partially coupled. In contrast, recent density-functional theory+dynamical mean-field theory (DFT+DMFT) calculations, supported by in situ X-ray diffraction (XRD) and X-ray emission spectroscopy (XES) measurements in laser-heated diamond anvil cells (LH-DACs), have challenged this assumption (Greenberg et al, 2023). Those experiments report instead a gradual HS to a LS crossover within metallic FeO-B1, suggesting a decoupling between the two transitions even at high temperature. While such LH-DAC studies represent major advances in directly probing FeO’s spin state at high P-T conditions, they also highlight constraining factors that limit the number of data acquired and make it difficult to fully track the spin crossover experimentally, particularly at high temperatures. These contrasting results motivate a complementary experimental approach capable of extending the pressure-temperature range to fully probe the spin crossover.

Here, we employ dynamic laser-driven shock compression to access high pressure-temperature conditions along the principal Hugoniot that extend well beyond the P-T range reached in static compression experiments. We report results from two experimental campaigns on FeO. First, we extended the Hugoniot curve of FeO up to ~ 900 GPa. Secondly, using in situ XRD and XES, we directly tracked both the structural and the iron-spin state evolution up to 261 GPa along the Hugoniot. Our experimental investigations were conducted on a $\text{Fe}_{0.90}\text{O}$ sample—referred to as FeO hereafter (details in supplementary material). Experiments were performed at the LULI2000 laser facility of the *Laboratoire pour l'Utilisation des Lasers Intenses* (Institut Polytechnique de Paris, France) and at the Matter in Extreme Conditions (MEC) end-station (Glenzer et al, 2016; Nagler et al, 2015) of the Linac Coherent Light Source (LCLS) at SLAC National Accelerator Laboratory.

Results and discussion

Hugoniot measurements

We extended the FeO Hugoniot to near-terapascal pressures by performing 5 laser-driven shock compression experiments at LULI200, spanning from 176 GPa to 871 GPa (Fig. 1, Table 1 and S3). This significantly expands the range of previous Hugoniot measurements (Yagi et al, 1988; Jeanloz and Ahrens, 1980) to near-terapascal pressures. To determine the compression state in the FeO sample, we used the impedance matching technique (Brygoo et al, 2015; Zel'Dovich and Raizer, 1966). The α -quartz window and aluminum pusher layer were used as reference materials for the impedance matching analysis. The α -quartz served as a transparent witness, which enable direct measurements of the shock velocity, allowing to perform the impedance matching at the both the Al-quartz and Al-FeO interfaces. Details on the experimental configurations and data analysis procedure are provided in the Methods and Supplementary Materials.

Table 1 Hugoniot result for Fe_xO ($x = 90$) including the target thickness (D), the shock velocity (U_S), particle velocity (U_P), pressure (P), and density (ρ). The FeO’s initial density of this study is $\rho_0=5.73 \text{ g/cm}^3$.

Shot n°	D^{FeO} (μm)	U_S^{quartz} (km/s)	U_S^{FeO} (km/s)	U_P^{FeO} (km/s)	P_H^{FeO} (GPa)	ρ^{FeO} (g/cm^3)
1	70	19.40 ± 0.17	16.69 ± 0.87	9.13 ± 0.26	871 ± 30	12.88 ± 1.3
2	67	19.10 ± 0.12	16.60 ± 0.68	8.90 ± 0.20	846 ± 22	12.44 ± 0.91
35	63	13.33 ± 0.42	12.01 ± 0.90	5.57 ± 0.32	382 ± 23	10.90 ± 1.27
40	64	16.25 ± 0.38	14.00 ± 0.97	7.23 ± 0.38	578 ± 33	12.16 ± 1.63
73 ¹	65	-	8.85 ± 0.58	3.47 ± 0.52 ¹	176 ± 29	9.42 ± 0.99
279	43	-	9.58 ± 0.22	3.70 ± 0.17 ¹	196 ± 10	9.33 ± 0.3

¹from FeO free-surface measurement

Measurements of U_P-U_S (particle velocity–shock velocity) and ρ -P (density–pressure) for shocked FeO are presented in Fig. 1, together with previously published data (Yagi et al, 1988; Jeanloz and Ahrens, 1980). The initial density is a critical parameter in determining a material’s Hugoniot. Our FeO sample has a different stoichiometry compared to previous work (Jeanloz and Ahrens (1980): $x=0.94$; Yagi et al (1988): $x=0.91$ and 0.95 ; and this study: $x=0.90$). In addition, to account for sample porosity in Jeanloz and Ahrens (1980), we recalculated the initial and shocked densities as detailed in the Supplementary Materials, section 2.2 and Table S1. Previous studies provide no evidence that small stoichiometric differences significantly affect the Hugoniot. Additionally, the discontinuous density increase near 70 GPa reported in earlier studies (Yagi et al, 1988; Jeanloz and Ahrens, 1980) was not reproduced in static compression experiments. Although the origin of this discontinuity has been debated and attributed to various processes (Jackson et al, 1990; Jackson and Ringwood, 1981), including a phase transition (Fei and Mao, 1994; Jeanloz and Ahrens, 1980) or metallization (Fischer et al, 2011a; Knittle and Jeanloz, 1986; Knittle et al, 1986), we follow previous work Young et al (2021) and consider only data above this discontinuity ($P > 73 \text{ GPa}$; $U_P > 1.8 \text{ km/s}$ and $\rho > 7.8 \text{ g/cm}^3$), since our lowest measured pressure exceeds this threshold (82 GPa; see Table S2).

In Fig. 1, the measured U_P-U_S and ρ -P relationship are compared with the earlier gas-gun experiments and its high-pressure extrapolation (Yagi et al, 1988; Jeanloz

and Ahrens, 1980). In the limited range where the datasets overlap ($3.5 < U_P < 4$ km/s, corresponding to $P \sim 200$ GPa), our measurements are in good agreement with the gas-gun results. At higher pressures, however, our measurements diverge from a simple extrapolation of the gas-gun results, underscoring the importance of direct experimental constraints. Our laser-driven shock experiments extend to substantially higher-pressure and reveal lower shock velocities at a given particle velocity, defining

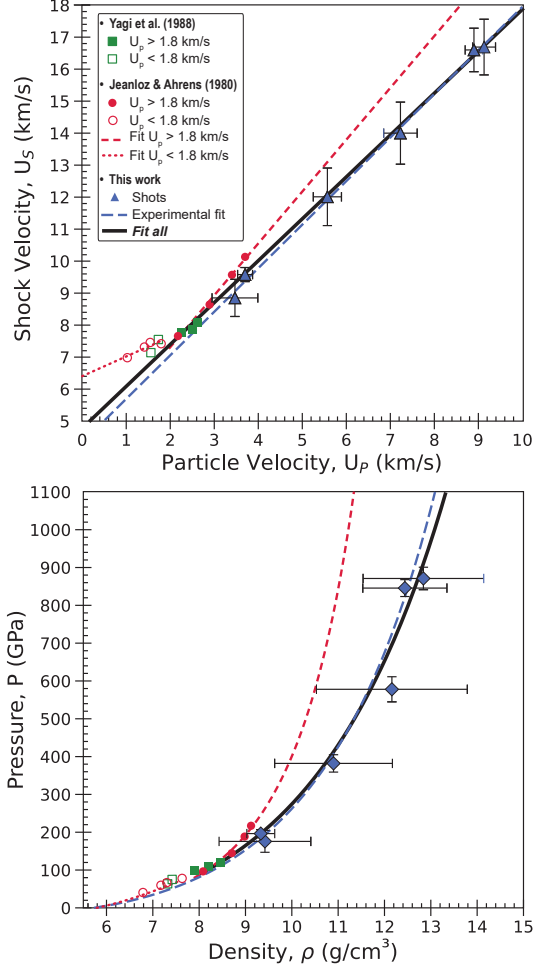


Fig. 1 FeO principal Hugoniot relationship in (left): shock velocity (U_S)-particle velocity (U_P) relationship and (right) pressure-density (P - ρ) relationship. Experimental data from this work (blue triangle) are fitted together with Jeanloz and Ahrens (1980) (red circle), and Yagi et al (1988) (green square) data from $U_P > 1.8$ km/s (black line). The red and blue dashed lines are the fit Jeanloz and Ahrens (1980)'s data only and the data from this study only, respectively

a higher-density Hugoniot than previously projected. These results highlight the need of our direct high-pressure measurements to robustly constrain the FeO Hugoniot.

Importantly, shot #279 provides an absolute equation of state measurement, for which both the U_P and the U_S were independently determined: U_P from the FeO free-surface velocity using the approximation $U_{fs} = 2U_P$, valid at moderate pressures (Zel'Dovich and Raizer, 1966) and U_S from the shock transit time, respectively. This enables a direct determination of the FeO pressure using the Rankine-Hugoniot relations without relying on the impedance matching. This data point is in good agreement with both the other measurement from this study, and the previously published gas-gun data, validating the high-pressure Hugoniot path reported here.

Combining our results with the lower pressure data, the FeO Hugoniot is described by a U_P - U_S relationship: $U_s = s * U_p + C_0$ with $s = 1.3089 (\pm 0.12)$ and $C_0 = 4.7775 (\pm 0.59)$, for $U_p \geq 1.8$ km/s.

X-ray measurements

In situ X-ray diffraction (XRD) and X-ray emission spectroscopy (XES) measurements during the shock compression were performed at the Matter in Extreme Conditions (MEC) end-station of the Linear Coherent Linac Source (LCLS) at SLAC National Accelerator Laboratory. This configuration, recently applied to dense silicate (Shim et al, 2023), enabled us to track both structural changes and spin state evolution in situ.

Simultaneous XRD and XES measurements could be performed on shocked FeO at 9 keV. To extend the Q-range of the XRD, additional shots (runs 529, 635, and 638; see Table S2) were acquired at 17 keV X-ray energy (Fig. 2), though at the expense of XES. The 9 keV XRD data were inconclusive due to self-absorption from the unshocked sample layer. Indeed, to ensure accurate XES measurements, the signal was collected from the drive laser side at a 60° angle. In this configuration, the XFEL

probe was timed so that the emission signal was acquired within the first $\sim 20 \mu\text{m}$ of shock propagation into the sample. This ensured a homogeneous compression state and minimized release effects, but with total sample thicknesses ranging from >30 to $50 \mu\text{m}$, the transmitted XRD signal had to pass through an additional $10\text{--}30 \mu\text{m}$ of

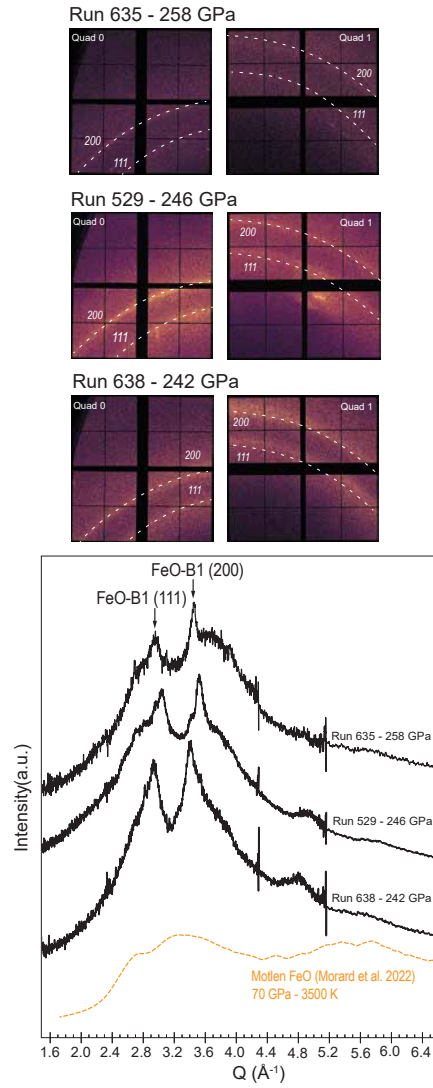


Fig. 2 X-ray diffraction images from Q0 (2θ : 15° to 35° and Q-range: 22 to 50 nm^{-1}) and Q1 (2θ : 19° to 28° and Q-range: 13 to 40 nm^{-1}) from ePix 10k detectors and 2D integrated patterns from Q0, Q1, and Q2 at 17 keV for run 638 - 242 GPa , run 529 - 246 GPa , and run 635 - 258 GPa . The orange dashed line is the FeO liquid structure factor from [Morard et al \(2022\)](#)

unshocked FeO before reaching the detector. Since the attenuation length of FeO is only $\sim 10 \mu\text{m}$ at 9 keV (compared to $\sim 40 \mu\text{m}$ at 17 keV), the self-absorption attenuated significantly the 9 keV XRD signal, preventing reliable interpretation of the solid phase's signal.

In contrast, XRD at 17 keV clearly revealed the persistence of the high-pressure FeO-B1 structure at $>242 \text{ GPa}$ along the principal Hugoniot (Fig. 2). Alongside the solid B1 peaks, two broad diffuse scattering features at $Q = 2.93 \text{ \AA}^{-1}$ and $Q = 3.4 \text{ \AA}^{-1}$ are observed (Fig. 2), consistent with the loss of long-range order. Such diffuse scattering may reflect either melting or rapid amorphization under nanosecond compression, with no evidence for a structural transition to the B2 phase (Coppari et al, 2021; Fischer et al, 2011b; Ozawa et al, 2011b; Murakami et al, 2004; Mao et al, 1996). Because diffusion and segregation require longer timescales than the nanosecond timescales in laser-driven shocks, metastable or amorphous states can persist beyond their equilibrium stability fields, potentially explaining the survival of B1 peaks above 242 GPa. This kinetic effect, together with the lack of direct shock temperature measurements makes detection of melting along the Hugoniot challenging, as the loss of Bragg peaks and the emergence of diffuse scattering can also arise from amorphization, especially in crystalline samples.

Despite these uncertainties, the persistence of FeO-B1 up to 258 GPa occurs well above the pressures where the previous FeO Hugoniots reported by Jeanloz and Ahrens (1980) intersect published melting curves (between 140 and 180 GPa) (Fu and Hirose, 2024; Dobrosavljevic et al, 2023; Morard et al, 2020; Komabayashi, 2014; Fischer and Campbell, 2010). Our experimental configuration does not allow for direct shock temperature measurements, and differences in starting material stoichiometry and initial density are expected to affect Hugoniot temperatures. Moreover, given the significant divergence between the high-pressure extrapolation of Jeanloz and Ahrens (1980)

Hugoniot and the Hugoniot measured in this study (Fig. 1) makes it not straightforward to apply their temperature estimates, especially when extrapolated beyond the experimental range.

Nevertheless, the diffuse scattering features observed above 242 GPa resemble those observed in static compression experiments of molten FeO (Fig.2)(Morard et al, 2022), supporting a melting interpretation. We therefore suggest that FeO along the Hugoniot has a regime of solid-liquid coexistence above 240 GPa, although a contribution from hot amorphous states cannot be excluded.

In situ XES enabled direct probing of the iron spin state under shock compression. The HS reference spectrum at ambient conditions shows a main $K\beta_{1,3}$ peak and a lower-energy satellite peak ($K\beta'$) (Fig. 3). Upon compression, the $K\beta_{1,3}$ peak systematically shift toward lower energies, while the $K\beta'$ peak intensity progressively decreases (Fig. 3).

To estimate the spin state evolution, we applied the Integrated Absolute Difference (IAD) method (Vankó et al, 2006). In the absence of a well-characterized LS FeO reference spectrum under comparable conditions, we refrained from using a LS reference from another Fe-bearing mineral, as the difference in host chemistry and Fe valence state could introduce large uncertainties. Instead, we adopted a relative approach using the same HS reference spectrum for each experimental campaign to ensure consistency (Fig. 3). For each spectrum, the HS reference was subtracted from the shocked spectrum, and the absolute value of the difference curve was integrated over the energy range, resulting in the IAD value. A larger IAD value—larger shaded areas—represents a greater difference from the HS reference and hence a higher LS fraction. The observed spectral evolution (Fig. 3), including the disappearance of $K\beta'$ peak and the systematic shift of the $K\beta_{1,3}$ main peak to lower energy, together with the continuous rise in IAD values with pressure (Fig. 4), indicates a continuous spin crossover along the Hugoniot up to 200-250 GPa.

Previous work by [Albers et al \(2022b\)](#) has shown that pressure-induced structural distortion can shift and broaden the main $K\beta_{1,3}$ line, thereby affecting the IAD. In such cases, the IAD variation is not directly linked to spin transition but rather to changes in Fe-O bonding geometry/angles and in covalency. Consequently, the full-spectrum IAD (IAD $K\beta_{1,3}$ in Fig. 4) may include non-spin-related contributions. This effect is especially true if there is a structural transition, such as the B1 to rB1 distortion observed in FeO cold compression ([Albers et al, 2022b](#)). In contrast, along the

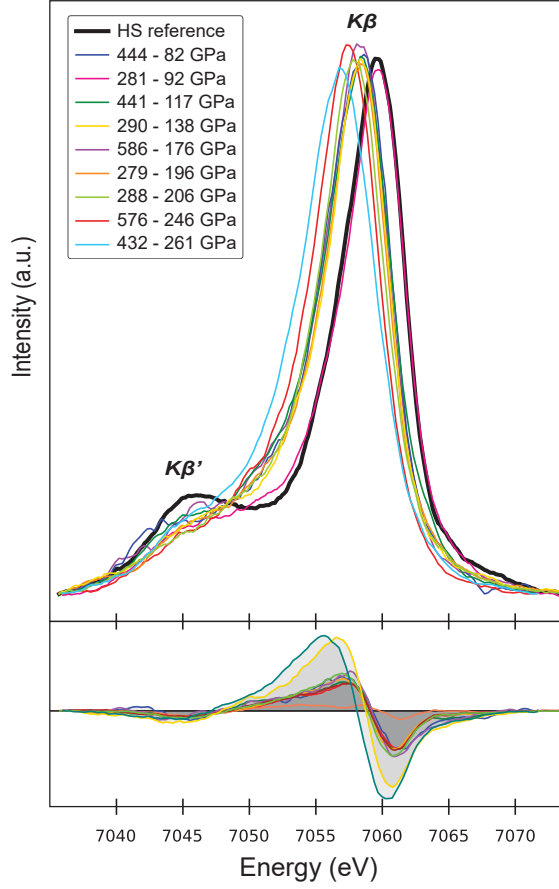


Fig. 3 Top: Fe $K\beta$ X-ray emission spectra collected from shocked FeO between 82 and 261 GPa. The black curve shows the HS reference spectrum at ambient pressure. **Bottom:** Difference curves between the reference and shocked spectra. The IAD (Integrated Absolute Difference) value ([Vankó et al, 2006](#)) corresponds to the integral of the absolute difference of the solid gray areas. Detailed thermodynamic conditions and IAD values for each shot are listed in Table S2 of the Supplementary Material. Separated XES spectra of all shots are shown in Fig. S4.

Hugoniot explored here, only the B1 structure and melting is expected, and our lowest reported pressure is already beyond the stability region of the rB1 phase. Nonetheless, to minimize the possible structural influences, we also evaluated the IAD restricted to the $K\beta'$ satellite region (IAD $K\beta'$ satellite in Fig. 4). To do so, we first aligned the XES spectra to the main $K\beta_{1,3}$ peak and integrated the absolute difference over the satellite region to capture changes specific to the satellite feature, which has been demonstrated to directly track the Fe spin moment, as its total loss of intensity indicates full LS Fe (Badro et al, 1999). Thus, the $K\beta'$ satellite only-IAD provides an additional, more selective indicator of spin crossover, removing potential pressure-induced effects. In Fig. 4, both IAD evaluations show a consistent, continuous trend with pressure, indicating a progressive increase of the LS fraction with pressure along

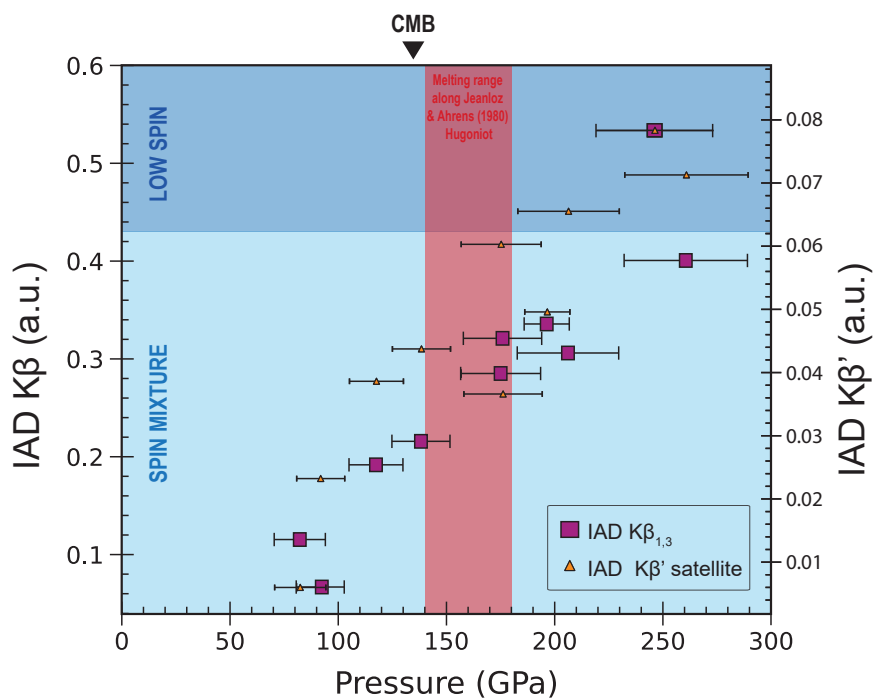


Fig. 4 Estimated IAD values (Vankó et al, 2006) as a function of pressure for shocked FeO. Estimated LS IAD values are indicated by the darker blue area from $K\beta'$ peak disappearance. Red areas indicate the estimated pressure where the melting curves (Fu and Hirose, 2024; Fischer and Campbell, 2010; Morard et al, 2020; Komabayashi, 2014) crosses Jeanloz and Ahrens (1980)'s Hugoniot.

the Hugoniot. The agreement between both the full IAD and the satellite only-IAD confirms that the observed spectra evolution is dominated by change in the spin state rather than structural effects.

At the highest pressures reached in this study, the systematic shift of the $K\beta_{1,3}$ main peak together with the near-complete disappearance of the $K\beta'$ satellite peak (Fig. 3) indicate that Fe approaches a full LS state (Badro et al, 1999). In the absence of an experimentally measured LS FeO spectrum under comparable conditions, we simulated Fe XES spectra using the code Quanta (Haverkort, 2016), allowing a direct visual comparison with our experimental data (Fig. 5). Details about the simulations can be found in the Supplementary Materials. Two of spectra (e.g., #576 at 246 GPa and #288 at 206 GPa) show near-complete loss of the $K\beta'$ feature, whereas our highest pressure spectrum (432 at 261 GPa) exhibits the furthest energy shift of the $K\beta_{1,3}$

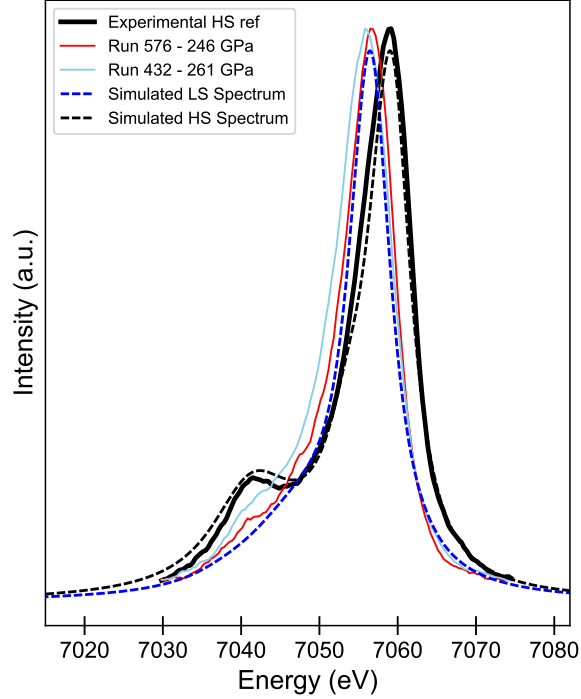


Fig. 5 Comparison of the experimental spectra with simulated high-spin (HS, black dashed) and low-spin (LS, blue dashed) Fe emission spectra shows. Shocked spectra at 246–261 GPa closely matches the LS simulation, indicating that Fe in FeO approaches a fully low-spin state under these conditions.

main peak but still retains a discernible $K\beta'$ shoulder (Fig. 3, 5 and S4). Comparison with the LS simulated spectra clearly shows the residual $K\beta'$ intensity in our highest pressure spectra (Fig. 5). This comparison reinforces that our experimental spectra follow a continuous spin crossover, with the fraction of LS Fe increasing progressively with pressure and reaching a full LS state at >260 GPa. Calculation of the full IAD using the simulated HS and LS spectra yields a value of 0.43, which can be taken as a quantitative reference for full LS state. This suggests that FeO under CMB conditions contains approximately 50 to 55% of LS Fe.

Our results significantly extend the pressure-temperature conditions of the measured spin transition in FeO. Previous cold-compression experiments reported the sluggish nature of the spin crossover at ambient temperature which begins at ~ 70 - 80 GPa in the rB1 phase and potentially reaching a full LS state between ~ 120 and 200 GPa in the B8 phase (Greenberg et al, 2023; Albers et al, 2022b; Hamada et al, 2016; Ozawa et al, 2011a; Mattila et al, 2007; Badro et al, 1999; Pasternak et al, 1997).

Recently, Greenberg et al (2023), investigated the spin-crossover at high-temperature. Their DFT+DMFT calculations (Fig. 1 in Greenberg et al (2023)) predict the onset of spin crossover in FeO-B1 at ~ 70 GPa near 1500 K, shifting to ~ 125 GPa at around 4000 K, and the full LS state reached at ~ 100 GPa at 1500 K and ~ 170 GPa at 4000 K. These results support the persistence of HS FeO-B1 at CMB conditions. Similarly, our XES measurements along the Hugoniot also suggest the persistence of a mixed-spin state in FeO, with HS iron still present at pressures relevant to the CMB (~ 135 GPa) at high temperature. In contrast, Greenberg et al (2023) experimental XES results (Fig. 5 in Greenberg et al (2023)) suggest a different trend, with a mixed-spin state ($\sim 60\%$ HS fraction) at 110 GPa and 1650 K but do not extend to higher pressures relevant to the CMB, leaving the calculations untested experimentally. Our XES measurements along the Hugoniot directly addressed this gap, measuring a LS fraction of 50 to 55% at at CMB conditions (~ 135 GPa). A

qualitative comparison with the XES spectra of [Greenberg et al \(2023\)](#) is provided in supplementary material, (Fig. S6), together with a discussion of the limitations.

The divergence between calculated and experimental results in [Greenberg et al \(2023\)](#) study likely reflects technical challenges inherent to LH-DAC experiments: the small scattering volume requires long acquisition times (minutes to tens of minutes per spectrum), stable laser heating, and precise alignment of the probed and heated areas to minimize the effect of thermal gradients. In addition, the XES signal is collected at 90° through an X-ray-transparent Be gasket, probing the entire sample across pressure—and, when heated, temperature—gradients, potentially obscuring the LS signature. Together, these factors complicate high-temperature XES measurements, explaining their limited availability ([Greenberg et al, 2023](#); [Kaa et al, 2022](#); [Albers et al, 2023, 2022a,b](#)).

The role of temperature is central in the spin transition, as elevated temperatures generally shift the spin transition toward higher pressures. Accordingly, in our shock compression experiments, the spin state is likely influenced by the extreme temperatures reached along the Hugoniot. A comparable temperature-dependent trend has been reported in ferropericlase, where the spin crossover occurs over a narrower pressure range at room temperature but broadens and shifts to higher pressures at high temperature (e.g., ([Trautner et al, 2024](#); [Sun et al, 2022](#); [Yang et al, 2021](#); [Wu et al, 2009](#); [Tsuchiya et al, 2006](#))). Our XES spectra suggest that a full LS state is nearly achieved above 240 GPa along the Hugoniot, suggesting that at lower temperatures, such as those expected at the Earth’s outer-core, a full LS state is likely achieved at similar pressure. However, the experimental results of [Greenberg et al \(2023\)](#) show a non-uniform temperature effect on the spin state: below 80 GPa, higher temperatures increase the LS fraction, whereas at 90 GPa the opposite trend is observed, with $\sim 67\%$ HS-Fe at ~ 1800 K and a fully HS state at ~ 2050 K. This discrepancy may reflect the

experimental challenges of probing XES at high temperatures, as discussed earlier, or illustrate a more complex interplay of pressure, temperature and electronic state.

Such electronic temperature-dependent behavior has also been suggested in the recent theoretical work by [Ho et al \(2024\)](#). They demonstrated that the IMT in FeO is temperature-dependent. According to their eDMFT calculations, at low temperature ($T \leq \sim 370\text{K}$) FeO undergoes a sharp transition from Mott insulator to metal. In contrast, at high temperature ($>2000\text{ K}$) the IMT is not direct, FeO exists in an intermediate quantum-critical state, where the e_g gap closes only at higher compression, which drives metallization and simultaneously initiates the spin crossover at ~ 140 to 150 GPa . However, at these pressures, our experimental results already attest to ~ 50 to 60% of LS Fe.

Even though the degree of coupling between these transitions remains uncertain, the continuous spin crossover observed here is robustly supported by our data and provides a foundation for considering its broader geophysical consequences. The HS to LS transition, through its 20 to 40% reduction in iron ionic volume, directly affects FeO's bulk modulus and thus produces abrupt changes in the seismic wave velocity. Similar to ferropericlase, where the spin transition modifies the bulk modulus, the crossover in FeO has the potential to generate depth-dependent seismic anomalies such as those observed at the CMB ([Trautner et al, 2023](#); [Lin et al, 2013](#)). However, the broad transition interval observed in this study, relevant to much of the Earth's mantle and core, also suggests that the spin-state-related effects occur progressively with depth. Consequently, the geophysical and geochemical impacts might be distributed over a wide pressure range, rather than localized to a narrow depth range in the Earth's mantle.

Although direct links between the FeO end-member spin state and mantle mineral properties are not straightforward, our results imply that HS iron would persist

in FeO-rich melts trapped at the base of the lower mantle at the end of the mantle crystallization (Boukaré et al, 2025, 2015). Changes in spin state may also affect iron partitioning between metal and silicate phases and/or between solid and liquid, potentially influencing both mantle and core evolution. Continued efforts to connect electronic transitions to mantle dynamics, phase equilibria, and transport properties are essential to improve geodynamic models. Moreover, the spin-state behavior reported here provides an important benchmark for future ab initio calculations. In particular, constraining the role of FeO in Fe–FeO liquid mixing (Komabayashi, 2014) and its associated electronic properties will be key to fully assess its impact on deep Earth’s core processes.

Methods

Sample characterization

The Fe_{1-x}O sample was purchased from Mateck Material and characterized by single crystal XRD X-ray diffraction at the Institute of Mineralogy, Physics of Materials, and Cosmochemistry (IMPMC) in Paris. The Fe_xO ($x = 0.9$) stoichiometry was determined following the relationship established in McCammon and Liu (1984). Refined lattice parameters are provided in Supplementary Table S1. The FeO targets were between 40 and 70 μm thick.

Laser-driven shock compression experiments

LULI2000 experiments

Flat-top pulses (5 or 10 ns duration) of the high-energy drive laser were focus on the target to a 500 μm -diameter focal spot using a continuous phase plate. Target consisted of a 10 μm -thick plastic (CH) ablator and a 40 μm -thick aluminum layer, which served to reduce pre-heating and act as a pusher to generate a uniform shock wave.

Mounted onto the aluminum layer in a side-by-side configuration were an α -quartz (54 to 108 μm thick, $\rho_0=2.65\text{ g/cm}^3$) and the FeO sample (60 to 74 μm thick), separated by a $\sim 50\text{ }\mu\text{m}$ gap (Fig 6a and b). Because FeO is opaque, its thermodynamic conditions during the shock compression were determined by impedance matching technique (Brygoo et al, 2015; Zel'Dovich and Raizer, 1966), using the α -quartz and aluminum layer used as reference materials (Desjarlais et al, 2017; Knudson and Desjarlais, 2013; Hicks et al, 2005). Under shock compression, a reflecting shock front is generated in the α -quartz, allowing direct measurement of the shock velocity in quartz (U_S^{quartz}) at the Al/quartz interface using the time-resolved velocimetry diagnostic VISAR (Velocity Interferometer System for Any Reflector)(Barker and Hollenbach, 1965, 1970, 1972). The thermodynamic conditions in the aluminum layer are given by the intersection between the quartz Hugoniot at known U_P^{quartz} and the reverse Hugoniot of Al as an approximation of its release isentrope (Fig. S1). Once the thermodynamic state of aluminum was established, we applied the impedance matching at the aluminum/FeO interface. Since FeO has a higher impedance than aluminum, the shock wave propagating from the aluminum into the FeO sample is partially reflected at the interface and propagated backward, reshocking the aluminum. The conditions in FeO are then given by the intersection between the reversed Hugoniot of Al and the Rayleigh line of FeO. The Rayleigh line is constructed using the initial density and the mean shock velocity in FeO ((\bar{U}_S^{FeO})), which is determined from the sample thickness and the shock transit time through the FeO layer. The transit time (Δt) is obtained by measuring the difference between the shock breakout times in the Al and FeO layers (Fig. 6b). To ensure reliable measurements of the mean shock velocity, each target was individually characterized and its thickness accurately measured. In addition, both the target design and laser pulse were optimized to produce a steady shock. Shock stationarity was monitored using a quartz witness positioned next to the sample (Fig. 6a), in which the instantaneous shock velocity was measured. As shown in

(Fig. 6b), the shock remains highly stationary in the quartz witness. This observation, together with the planarity of the shock front, provides confidence in the reliability of the mean shock velocity measurements. A small gap between the sample and the quartz witness enabled direct and unambiguous identification of the shock breakout time from the Al layer. This geometry also allowed the contribution of the glue layer to be assessed and shown to be negligible due to its minimal thickness. Uncertainties were estimated using a Monte Carlo approach (10000 iterations per data point), accounting for uncertainties in the quartz shock velocity, the mean shock velocity in FeO, and the initial sample density. A schematic impedance match construction is provided in the Fig. S1. Here, we report 5 shots from the LULI2000 facility (Table 1 and Supplementary Table S3).

MEC experiments

At the Matter in Extreme Conditions (MEC) end station of LCLS, in situ X-ray diffraction (XRD) and X-ray emission spectroscopy (XES) measurements were performed during the shock compression. The frequency-doubled Nd:glass drive laser delivered flat-top temporal pulses with a duration of 8 ns and a 300 μm focal spot on the target, shaped using a continuous phase plate. The targets consisted of a 79 μm -thick polyimide ($\text{C}_{22}\text{H}_{10}\text{N}_2\text{O}_5$, also known as black Kapton) ablator, coated with a 300 nm layer of aluminum, onto which the FeO sample was glued. Two target configurations were used: (*i*) a “full” design, in which the FeO fully covered the underlying layers, or a (*ii*) “step” configuration, which allowed direct observation of the shock breakout in the Black Kapton on the VISAR image (Fig 6d). A total of 13 shots were carried out over laser energies of 15 to 73 J, generating pressure from 82 and 261 GPa on the FeO Hugoniot (Table S2).

The X-ray probing was timed at various delays, ranging from 8 to 15 ns with respect to the optical laser pulse, to ensure that the measurement occurred while the shock front was propagating approximately in the first 20 nm into the FeO sample.

The hydrodynamics were monitored with the VISAR system operating at 532 nm. Several approaches were used to determine the pressure and density of the shocked FeO at MEC:

- a.) For targets with a step design, the shocked properties of FeO were determined by impedance matching from Black Kapton to FeO, using the mean shock velocity in Black Kapton: $\bar{U}_S^{BK} = d_{BK} / \Delta t$ where d is the Black Kapton thickness and Δt the transit times, together with the SESAME equation of state for parylene (SESAME

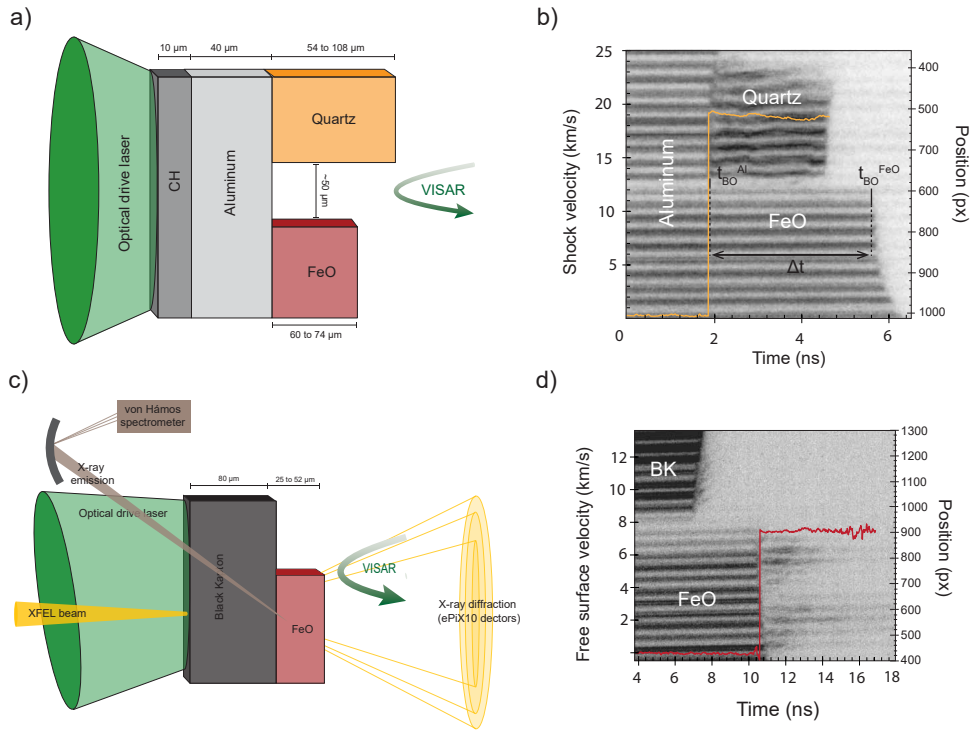


Fig. 6 Schematic experimental setup: a) Target designs for FeO Hugoniot measurements at LULI2000. b) VISAR record from shot 2 using target design from a) with the extracted shock velocity profiles superposed on the VISAR image. The shock velocity in quartz is determined from the shift in the fringe pattern. FeO is opaque, resulting in no fringe motion being observed in the bottom part of the VISAR image. The mean shock velocity (\bar{U}_S^{FeO}) from the shock transit time in FeO (Δt) calculated by measuring the difference in the breakout times between Al (t_{BO}^{Al}) and FeO (t_{BO}^{FeO}). c) Schematic representation of the experimental setup geometry at the MEC end station. d) VISAR record from shot 279 using target design from c) with the extracted free-surface velocity profiles superposed on the VISAR image.

7770) evaluated at the density of Black Kapton. This approach was preferred over the direct determination of the \overline{U}_S^{FeO} , to account for the limited accuracy of the FeO thickness determination during the first experimental campaign. In contrast, Black Kapton is reproducible and thickness was well characterized prior the first campaign, providing a more reliable determination of the shock FeO conditions.

- b.)** For the targets with a full design or with a step not visible on the VISAR image, i.e., for which the breakout of the Black Kapton could not be read, the transit time could not be used to determine the shocked conditions of FeO. Therefore, the determination of the FeO pressure relied on a calibration between the Black Kapton's ablation pressure and the laser drive energy at MEC. For this calibration, the Black Kapton ablation pressure was obtained by measuring its mean shock velocity (\overline{U}_S^{BK}) from transit times, following the same procedure as in step a.). The dataset comprised all the shots from the same LCLS campaign (L10020) that employed the same phase plate (300) and pulse duration (8ns), where the breakout of Black Kapton was clearly visible in the VISAR images. In total, 81 shots were used for this calibration. Once the \overline{U}_S^{BK} is obtained, the Black Kapton particle velocity and pressure (U_P^{BK} and $PP_{ablation}^{BK}$) can be calculated using its equation of state. The impedance matching is then applied for the determination of the FeO shocked state. A schematic representation of the impedance match construction is provided in Fig. S3. The laser drive energy vs Black Kapton ablation pressure calibration is plotted in Fig. S4.
- c.)** For a couple of targets (runs 441 and 444), a LiF window was glued onto the FeO sample to monitor the FeO/LiF interface velocity. These targets were shot during our first campaign, for which the FeO sample thickness could not be determined with sufficient accuracy. As a result, we chose not to use the LiF measurements to track the particle velocity, as the thickness uncertainty prevented a reliable assessment

of shock decay. We emphasize that such release effects were avoided in the X-ray measurements by probing the sample sufficiently early during shock propagation.

- d.) Lastly, for the low-pressure shots below melting—where reflectivity in the sample was still maintained—the particle velocity (U_P^{FeO}) was inferred from the free-surface velocity (U_{fs}^{FeO}) of the FeO, using the approximation $U_{fs} = 2U_P$, valid at moderate pressures (Zel'Dovich and Raizer, 1966). Once the FeO shocked states were determined from U_S^{FeO} , U_P^{FeO} , and ρ_0^{FeO} . This procedure was applied to one shot (#279 - Fig. 6d) conducted during our second MEC campaign, and for which the sample thickness was better characterized than during the first campaign. Because both U_P^{FeO} and U_S^{FeO} were directly measured for this shot, from free-surface velocity and transit time respectively, the pressure was determined using the Rankine-Hugoniot relations without relying on impedance matching, providing an absolute measurement of the FeO shock state. This shot was therefore included in the Hugoniot determination (Fig. 1).

The uncertainties from the impedance matching were propagated using a Monte Carlo approach (10000 iterations per data point), accounting for uncertainties in the Black Kapton pressure, the mean shock velocity in FeO, and the initial densities of all materials. Pressure was obtained by impedance matching between Black Kapton and FeO, for $U_P > 3.8 \text{ km.s}^{-1}$, the Black Kapton reshock state was calculated using the symmetric Hugoniot derived from the SESAME equation of state for parylene (table #7770). Detailed extended data can be found in Table S2.

X-ray diagnostics

During the shock compression, the samples were probed by a quasi-monochromatic incident X-ray beam set at either 8, 9, or 17 keV with a temporal pulse length of ~ 60 fs focused on the target to a spot size of $\sim 30 \mu\text{m}$ diameter FWHM. The X-ray spot size was smaller than the compressed layer region, which limited the pressure and

temperature gradients in the probed area in the sample. A reference measurement was collected prior to each shot, then the target was moved to a fresh spot for the real shot.

X-ray diffraction (XRD): The XRD signal was collected in the transmission geometry at 9 and 17 keV using four ePix10k detectors (Fig. 6c) (Blaj et al, 2015; Carini et al, 2016). No self-absorption corrections were applied to the XRD images. At this energy, the XRD setup covered an angular range of 9° to 75° 2θ , corresponding to a Q-range of 14 to 82 nm^{-1} . The Q0 (2θ : 15 to 35, Q-range: 22 to 50 nm^{-1}) and Q1 (2θ : 9 to 28, Q-range: 13 to 40 nm^{-1}) detectors were used for the analysis. The two-dimensional (2D) diffraction patterns were integrated using the Dioptas software (Prescher and Prakapenka, 2015), including sample-detector distance, polarization, and tilting, calibrated with CeO_2 .

X-ray emission spectroscopy (XES): XES signals were collected backward, on the drive laser side of the target (Fig. 6c), at 8 and 9 keV by a multocrystal energy dispersive spectrometer on a von Hamos geometry (Alonso-Mori et al, 2012). The details of the setup can be found in Shim et al (2023).

Data availability. The raw XRD, XES, and VISAR images used in this study will be made available on a Figshare repository after acceptance of the paper. The data analysis code for XES is available at <https://github.com/Xuehui-Wei/IXE>.

Supplementary information.

Acknowledgments. This work was supported by the ANR grant MIN-DIXI (ANR-22-CE49-0006). Dynamic compression experiments were performed at the MEC instrument of LCLS, supported by the US Department of Energy (DOE) Office of Science, Fusion Energy Science under contract SF00515 and FWP 100182 were supported by LCLS, a National User Facility operated by Stanford University on behalf of the US DOE, Office of Basic Energy Sciences. We thank the staff of LULI2000 for their support in conducting the experiments and Frederic Lefevre for target assembly. G.M., A.R., and L.L. would like acknowledge support from the CRNS travel grant

GoToXFEL. L.L. and G.M. thank H. Elnaggar for performing the HS–LS spin simulations, as well as S. Merkel and J. Chantel from the UMET laboratory (Lille) their support with target preparation. L.L. also thanks Ian Ocampo for fruitful discussions.

References

- Albers C, Sakrowski R, Libon L, et al (2022a) Fe³⁺-hosting carbon phases in the deep Earth - hosting carbon phases in the deep Earth. *Physical Review B* 105(8):085155. <https://doi.org/10.1103/physrevb.105.085155>
- Albers C, Thiering N, Sakrowski R, et al (2022b) Non-resonant and resonant X-ray emission at high pressure using a von Hámos setup: the case of FeO. *Journal of Physics: Conference Series* 2380(1):012128. <https://doi.org/10.1088/1742-6596/2380/1/012128>
- Albers C, Sakrowski R, Thiering N, et al (2023) High-efficient X-ray emission spectroscopy of cold-compressed Fe₂O₃ and laser-heated pressurized FeCO₃ using a von Hámos spectrometer. *Journal of Analytical Atomic Spectrometry* <https://doi.org/10.1039/d3ja00014a>, (in review)
- Alfè D, Price G, Gillan MJ (1999) Oxygen in the Earth's core: a first-principles study. *Physics of the Earth and Planetary Interiors* 110(3–4):191–210. [https://doi.org/10.1016/s0031-9201\(98\)00134-4](https://doi.org/10.1016/s0031-9201(98)00134-4)
- Alfè D, Gillan M, Price G (2002) Composition and temperature of the Earth's core constrained by combining ab initio calculations and seismic data. *Earth and Planetary Science Letters* 195(1–2):91–98. [https://doi.org/10.1016/s0012-821x\(01\)00568-4](https://doi.org/10.1016/s0012-821x(01)00568-4)
- Alonso-Mori R, Kern J, Gildea RJ, et al (2012) Energy-dispersive X-ray emission spectroscopy using an X-ray free-electron laser in a shot-by-shot mode. *Proceedings*

- of the National Academy of Sciences 109(47):19103–19107. <https://doi.org/10.1073/pnas.1211384109>
- Badro J, Struzhkin VV, Shu J, et al (1999) Magnetism in FeO at Megabar Pressures from X-Ray Emission Spectroscopy. *Physical Review Letters* 83(20):4101–4104. <https://doi.org/10.1103/physrevlett.83.4101>
- Badro J, Fiquet G, Guyot F, et al (2007) Effect of light elements on the sound velocities in solid iron: Implications for the composition of Earth's core. *Earth and Planetary Science Letters* 254(1–2):233–238. <https://doi.org/10.1016/j.epsl.2006.11.025>
- Barker LM, Hollenbach RE (1965) Interferometer Technique for Measuring the Dynamic Mechanical Properties of Materials. *Review of Scientific Instruments* 36(11):1617–1620. <https://doi.org/10.1063/1.1719405>
- Barker LM, Hollenbach RE (1970) Shock-Wave Studies of PMMA, Fused Silica, and Sapphire. *Journal of Applied Physics* 41(10):4208–4226. <https://doi.org/10.1063/1.1658439>
- Barker LM, Hollenbach RE (1972) Laser interferometer for measuring high velocities of any reflecting surface. *Journal of Applied Physics* 43(11):4669–4675. <https://doi.org/10.1063/1.1660986>
- Blaž G, Caragiulo P, Carini G, et al (2015) X-ray detectors at the Linac Coherent Light Source. *Journal of Synchrotron Radiation* 22(3):577–583. <https://doi.org/10.1107/s1600577515005317>
- Boukaré C, Ricard Y, Fiquet G (2015) Thermodynamics of the MgO-FeO-SiO₂ system up to 140 GPa: Application to the crystallization of Earth's magma ocean. *Journal of Geophysical Research: Solid Earth* 120(9):6085–6101. <https://doi.org/10.1002/2015jb011929>

- Boukaré CE, Badro J, Samuel H (2025) Solidification of earth's mantle led inevitably to a basal magma ocean. *Nature* 640(8057):114–119. <https://doi.org/10.1038/s41586-025-08701-z>
- Brygoo S, Millot M, Loubeyre P, et al (2015) Analysis of laser shock experiments on precompressed samples using a quartz reference and application to warm dense hydrogen and helium. *Journal of Applied Physics* 118(19). <https://doi.org/10.1063/1.4935295>
- Carini GA, Alonso-Mori R, Blaj G, et al (2016) ePix100 camera: Use and applications at LCLS. In: *AIP Conference Proceedings*. Author(s), <https://doi.org/10.1063/1.4952880>
- Cohen RE, Mazin II, Isaak DG (1997) Magnetic Collapse in Transition Metal Oxides at High Pressure: Implications for the Earth. *Science* 275(5300):654–657. <https://doi.org/10.1126/science.275.5300.654>
- Coppari F, Smith RF, Wang J, et al (2021) Implications of the iron oxide phase transition on the interiors of rocky exoplanets. *Nature Geoscience* 14(3):121–126. <https://doi.org/10.1038/s41561-020-00684-y>
- Desjarlais MP, Knudson MD, Cochrane KR (2017) Extension of the Hugoniot and analytical release model of α -quartz to 0.2–3 TPa. *Journal of Applied Physics* 122(3). <https://doi.org/10.1063/1.4991814>
- Dobrosavljevic VV, Sturhahn W, Jackson JM (2019) Evaluating the role of iron-rich (mg,fe)o in ultralow velocity zones. *Minerals* 9(12):762. <https://doi.org/10.3390/min9120762>
- Dobrosavljevic VV, Zhang D, Sturhahn W, et al (2023) Melting and defect transitions in FeO up to pressures of Earth's core-mantle boundary. *Nature Communications*

14(1). <https://doi.org/10.1038/s41467-023-43154-w>

Fei Y, Mao Hk (1994) In Situ Determination of the NiAs Phase of FeO at High Pressure and Temperature. *Science* 266(5191):1678–1680. <https://doi.org/10.1126/science.266.5191.1678>

Fischer RA, Campbell AJ (2010) High-pressure melting of wustite. *American Mineralogist* 95(10):1473–1477. <https://doi.org/10.2138/am.2010.3463>

Fischer RA, Campbell AJ, Lord OT, et al (2011a) Phase transition and metallization of FeO at high pressures and temperatures. *Geophysical Research Letters* 38(24):n/a–n/a. <https://doi.org/10.1029/2011gl049800>

Fischer RA, Campbell AJ, Shofner GA, et al (2011b) Equation of state and phase diagram of FeO. *Earth and Planetary Science Letters* 304(3-4):496–502. <https://doi.org/10.1016/j.epsl.2011.02.025>

Fu S, Hirose K (2024) Melting Behavior of B1 FeO up to 186 GPa: Existence of FeO-Rich Melts in the Lowermost Mantle. *Geophysical Research Letters* 51(9). <https://doi.org/10.1029/2023gl106475>

Glenzer SH, Fletcher LB, Galtier E, et al (2016) Matter under extreme conditions experiments at the Linac Coherent Light Source. *Journal of Physics B: Atomic, Molecular and Optical Physics* 49(9):092001. <https://doi.org/10.1088/0953-4075/49/9/092001>

Greenberg E, Nazarov R, Landa A, et al (2023) Phase transitions and spin state of iron in FeO under the conditions of Earth's deep interior. *Physical Review B* 107(24):l241103. <https://doi.org/10.1103/physrevb.107.l241103>

- Hamada M, Kamada S, Ohtani E, et al (2016) Magnetic and spin transitions in wüstite: A synchrotron Mössbauer spectroscopic study. *Physical Review B* 93(15):155165. <https://doi.org/10.1103/physrevb.93.155165>
- Haverkort MW (2016) Quanta for core level spectroscopy—excitons, resonances and band excitations in time and frequency domain. In: *Journal of Physics: Conference Series*, IOP Publishing, p 012001
- Hazen RM, Jeanloz R (1984) Wüstite (Fe_{1-x}O): A review of its defect structure and physical properties. *Reviews of Geophysics* 22(1):37–46. <https://doi.org/10.1029/rg022i001p00037>
- Hicks DG, Boehly TR, Celliers PM, et al (2005) Shock compression of quartz in the high-pressure fluid regime. *Physics of Plasmas* 12(8). <https://doi.org/10.1063/1.2009528>
- Hirose K, Sinmyo R, Hernlund J (2017) Perovskite in Earth’s deep interior. *Science* 358(6364):734–738. <https://doi.org/10.1126/science.aam8561>
- Ho WGD, Zhang P, Haule K, et al (2024) Quantum critical phase of FeO spans conditions of Earth’s lower mantle. *Nature Communications* 15(1). <https://doi.org/10.1038/s41467-024-47489-w>
- Jackson I, Ringwood AE (1981) High-pressure polymorphism of the iron oxides. *Geophysical Journal of the Royal Astronomical Society* 64(3):767–783. <https://doi.org/10.1111/j.1365-246x.1981.tb02694.x>
- Jackson I, Khanna SK, Revcolevschi A, et al (1990) Elasticity, shear-mode softening and high-pressure polymorphism of wüstite (Fe_{1-x}O). *Journal of Geophysical Research: Solid Earth* 95(B13):21671–21685. <https://doi.org/10.1029/jb095ib13p21671>

- Jackson JM, Thomas C (2021) Seismic and mineral physics constraints on the D" layer. *Mantle Convection and Surface Expressions* pp 193–227. <https://doi.org/10.1002/9781119528609.ch8>
- Jacobsen SD, Lin JF, Angel RJ, et al (2005) Single-crystal synchrotron X-ray diffraction study of wüstite and magnesiowüstite at lower-mantle pressures. *Journal of Synchrotron Radiation* 12(5):577–583. <https://doi.org/10.1107/s0909049505022326>
- Jeanloz R, Ahrens TJ (1980) Equations of state of FeO and CaO. *Geophysical Journal International* 62(3):505–528. <https://doi.org/10.1111/j.1365-246x.1980.tb02588.x>
- Kaa JM, Sternemann C, Appel K, et al (2022) Structural and electron spin state changes in an x-ray heated iron carbonate system at the Earth's lower mantle pressures. *Physical Review Research* 4(3):033042. <https://doi.org/10.1103/physrevresearch.4.033042>
- Knittle E, Jeanloz R (1986) High-pressure metallization of FeO and implications for the Earth's core. *Geophysical Research Letters* 13(13):1541–1544. <https://doi.org/10.1029/gl013i013p01541>
- Knittle E, Jeanloz R (1991) Earth's Core-Mantle Boundary: Results of Experiments at High Pressures and Temperatures. *Science* 251(5000):1438–1443. <https://doi.org/10.1126/science.251.5000.1438>
- Knittle E, Jeanloz R, Mitchell A, et al (1986) Metallization of Fe_{0.94}O at elevated pressures and temperatures observed by shock-wave electrical resistivity measurements. *Solid State Communications* 59(7):513–515. [https://doi.org/10.1016/0038-1098\(86\)90699-x](https://doi.org/10.1016/0038-1098(86)90699-x)
- Knudson MD, Desjarlais MP (2013) Adiabatic release measurements in α -quartz as a shock standard in the multimegabar regime. *Physical Review B* 88(18):184107.

<https://doi.org/10.1103/physrevb.88.184107>

Komabayashi T (2014) Thermodynamics of melting relations in the system Fe-FeO at high pressure: Implications for oxygen in the Earth's core. *Journal of Geophysical Research: Solid Earth* 119(5):4164–4177. <https://doi.org/10.1002/2014jb010980>

Labrosse S, Hernlund JW, Coltice N (2007) A crystallizing dense magma ocean at the base of the Earth's mantle. *Nature* 450(7171):866–869. <https://doi.org/10.1038/nature06355>

Leonov I (2015) Metal-insulator transition and local-moment collapse in FeO under pressure. *Physical Review B* 92(8):085142. <https://doi.org/10.1103/physrevb.92.085142>

Li X, Bykova E, Vasiukov D, et al (2024) Monoclinic distortion and magnetic transitions in FeO under pressure and temperature. *Communications Physics* 7(1). <https://doi.org/10.1038/s42005-024-01797-1>

Lin JF, Speziale S, Mao Z, et al (2013) Effects of the electronic spin transitions of iron in lower mantle minerals: Implications for deep mantle geophysics and geochemistry. *Reviews of Geophysics* 51(2):244–275. <https://doi.org/10.1002/rog.20010>

Manga M, Jeanloz R (1996) Implications of a metal-bearing chemical boundary layer in D'' for mantle dynamics. *Geophysical research letters* 23(22):3091–3094. <https://doi.org/10.1029/96GL03021>

Mao Hk, Shu J, Fei Y, et al (1996) The wüstite enigma. *Physics of the Earth and Planetary Interiors* 96(2–3):135–145. [https://doi.org/10.1016/0031-9201\(96\)03146-9](https://doi.org/10.1016/0031-9201(96)03146-9)

- Mattila A, Rueff JP, Badro J, et al (2007) Metal-Ligand Interplay in Strongly Correlated Oxides: A Parametrized Phase Diagram for Pressure-Induced Spin Transitions. *Physical Review Letters* 98(19):196404. <https://doi.org/10.1103/physrevlett.98.196404>
- McCammon C, Liu Lg (1984) The effects of pressure and temperature on nonstoichiometric wüstite, Fe_xO: The iron-rich phase boundary. *Physics and Chemistry of Minerals* 10(3):106–113. <https://doi.org/10.1007/bf00309644>
- McCammon CA, Ringwood AE, Jackson I (1983) Thermodynamics of the system Fe-FeO-MgO at high pressure and temperature and a model for formation of the Earth's core. *Geophysical Journal International* 72(3):577–595. <https://doi.org/10.1111/j.1365-246x.1983.tb02821.x>
- Morard G, Andrault D, Antonangeli D, et al (2017) Fe-FeO and Fe-Fe₃C melting relations at Earth's core-mantle boundary conditions: Implications for a volatile-rich or oxygen-rich core. *Earth and Planetary Science Letters* 473:94–103. <https://doi.org/10.1016/j.epsl.2017.05.024>
- Morard G, Hernandez JA, Guarguaglini M, et al (2020) In situ X-ray diffraction of silicate liquids and glasses under dynamic and static compression to megabar pressures. *Proceedings of the National Academy of Sciences* 117(22):11981–11986. <https://doi.org/10.1073/pnas.1920470117>
- Morard G, Antonangeli D, Bouchet J, et al (2022) Structural and Electronic Transitions in Liquid FeO Under High Pressure. *Journal of Geophysical Research: Solid Earth* 127(11). <https://doi.org/10.1029/2022jb025117>
- Murakami M, Hirose K, Kawamura K, et al (2004) Post-Perovskite Phase Transition in MgSiO₃. *Science* 304(5672):855–858. <https://doi.org/10.1126/science.1095932>

- Nagler B, Arnold B, Bouchard G, et al (2015) The Matter in Extreme Conditions instrument at the Linac Coherent Light Source. *Journal of Synchrotron Radiation* 22(3):520–525. <https://doi.org/10.1107/s1600577515004865>
- Nomura R, Ozawa H, Tateno S, et al (2011) Spin crossover and iron-rich silicate melt in the Earth's deep mantle. *Nature* 473(7346):199–202. <https://doi.org/10.1038/nature09940>
- Ohta K, Cohen RE, Hirose K, et al (2012) Experimental and Theoretical Evidence for Pressure-Induced Metallization in FeO with Rocksalt-Type Structure. *Physical Review Letters* 108(2):026403. <https://doi.org/10.1103/physrevlett.108.026403>
- Ohta K, Fujino K, Kuwayama Y, et al (2014) Highly conductive iron-rich (Mg,Fe)O magnesiowüstite and its stability in the Earth's lower mantle. *Journal of Geophysical Research: Solid Earth* 119(6):4656–4665. <https://doi.org/10.1002/2014jb010972>
- Ozawa H, Hirose K, Tateno S, et al (2010) Phase transition boundary between B1 and B8 structures of FeO up to 210 GPa. *Physics of the Earth and Planetary Interiors* 179(3–4):157–163. <https://doi.org/10.1016/j.pepi.2009.11.005>
- Ozawa H, Hirose K, Ohta K, et al (2011a) Spin crossover, structural change, and metallization in NiAs-type FeO at high pressure. *Physical Review B* 84(13):134417. <https://doi.org/10.1103/physrevb.84.134417>
- Ozawa H, Takahashi F, Hirose K, et al (2011b) Phase Transition of FeO and Stratification in Earth's Outer Core. *Science* 334(6057):792–794. <https://doi.org/10.1126/science.1208265>
- Pasternak MP, Taylor RD, Jeanloz R, et al (1997) High Pressure Collapse of Magnetism in Fe_{0.94}O: Mössbauer Spectroscopy Beyond 100 GPa. *Physical Review Letters* 79(25):5046–5049. <https://doi.org/10.1103/physrevlett.79.5046>

- Prescher C, Prakapenka VB (2015) DIOPTAS: a program for reduction of two-dimensional X-ray diffraction data and data exploration. *High Pressure Research* 35(3):223–230. <https://doi.org/10.1080/08957959.2015.1059835>
- Ringwood AE (1977) Composition of the core and implications for origin of the Earth. *Geochemical Journal* 11(3):111–135. <https://doi.org/10.2343/geochemj.11.111>
- Shim SH, Ko B, Sokaras D, et al (2023) Ultrafast x-ray detection of low-spin iron in molten silicate under deep planetary interior conditions. *Science Advances* 9(42). <https://doi.org/10.1126/sciadv.adi6153>
- Sun Y, Zhuang J, Wentzcovitch RM (2022) Thermodynamics of spin crossover in ferroperricite: an improved LDA + U calculation. *Electronic Structure* 4(1):014008. <https://doi.org/10.1088/2516-1075/ac522b>
- Trautner VE, Stackhouse S, Turner AR, et al (2023) Compressibility of ferroperricite at high-temperature: Evidence for the iron spin crossover in seismic tomography. *Earth and Planetary Science Letters* 618:118296. <https://doi.org/10.1016/j.epsl.2023.118296>
- Trautner VE, Rijal A, Plueckthun C, et al (2024) Iron content-dependence of ferroperricite elastic properties across the spin crossover from novel experiments and machine learning. *Geophysical Research Letters* 51(22). <https://doi.org/10.1029/2024gl111276>
- Tsuchiya T, Wentzcovitch RM, da Silva CRS, et al (2006) Spin Transition in Magnetite in Earth's Lower Mantle. *Physical Review Letters* 96(19):198501. <https://doi.org/10.1103/physrevlett.96.198501>
- Vankó G, Neisius T, Molnár G, et al (2006) Probing the 3d Spin Momentum with X-ray Emission Spectroscopy: The Case of Molecular-Spin Transitions. *The Journal*

- of Physical Chemistry B 110(24):11647–11653. <https://doi.org/10.1021/jp0615961>
- Wicks JK, Jackson JM, Sturhahn W (2010) Very low sound velocities in iron-rich (Mg,Fe)O: Implications for the core-mantle boundary region. *Geophysical Research Letters* 37(15). <https://doi.org/10.1029/2010gl043689>
- Wicks JK, Jackson JM, Sturhahn W, et al (2017) Sound velocity and density of magnesiowüstites: Implications for ultralow-velocity zone topography. *Geophysical Research Letters* 44(5):2148–2158. <https://doi.org/10.1002/2016gl071225>
- Wu Z, Justo JF, da Silva CRS, et al (2009) Anomalous thermodynamic properties in ferropicicase throughout its spin crossover. *Physical Review B* 80(1):014409. <https://doi.org/10.1103/physrevb.80.014409>
- Yagi T, Suzuki T, Akimoto S (1985) Static compression of wüstite ($\text{Fe}_{0.98}\text{O}$) to 120 GPa. *Journal of Geophysical Research: Solid Earth* 90(B10):8784–8788. <https://doi.org/10.1029/jb090ib10p08784>
- Yagi T, Fukuoka K, Takei H, et al (1988) Shock compression of Wüstite. *Geophysical Research Letters* 15(8):816–819. <https://doi.org/10.1029/gl015i008p00816>
- Yang K, Wang X, Zhang J, et al (2021) Entropic broadening of the spin-crossover pressure in ferropicicase. *Physical Review B* 103(22):224105. <https://doi.org/10.1103/physrevb.103.224105>
- Young G, Fan L, Zhao B, et al (2021) Equation of State for Fe-9.0 wt% O up to 246 GPa: Implications for Oxygen in the Earth's Outer Core. *Journal of Geophysical Research: Solid Earth* 126(2). <https://doi.org/10.1029/2020jb021056>
- Zel'Dovich YB, Raizer YP (1966) *Physics of shock waves and high-temperature hydrodynamic phenomena*. Academic Press, New York